Microwave Image Reconstruction From 3-D Fields Coupled to 2-D Parameter Estimation

Qianqian Fang*, *Student Member, IEEE*, Paul M. Meaney, *Member, IEEE*, Shireen D. Geimer, Anatoly V. Streltsov, and Keith D. Paulsen, *Member, IEEE*

***Abstract*—An efficient Gauss–Newton iterative imaging technique utilizing a three-dimensional (3-D) field solution coupled to a two-dimensional (2-D) parameter estimation scheme (3-D/2-D) is presented for microwave tomographic imaging in medical applications. While electromagnetic wave propagation is described fully by a 3-D vector field, a 3-D scalar model has been applied to improve the efficiency of the iterative reconstruction process with apparently limited reduction in accuracy. In addition, the image recovery has been restricted to 2-D but is generalizable to three dimensions. Image artifacts related primarily to 3-D effects are reduced when compared with results from an entirely two-dimensional inversion (2-D/2-D). Important advances in terms of improving algorithmic efficiency include use of a block solver for computing the field solutions and application of the dual mesh scheme and adjoint approach for Jacobian construction. Methods which enhance the image quality such as the log-magnitude/unwrapped phase minimization were also applied. Results obtained from synthetic measurement data show that the new 3-D/2-D algorithm consistently outperforms its 2-D/2-D counterpart in terms of reducing the effective imaging slice thickness in both permittivity and conductivity images over a range of inclusion sizes and background medium contrasts.**

***Index Terms*—Adjoint method, diffraction tomography, dual-mesh, Gauss–Newton method, microwave imaging, phase unwrapping.**

I. Introduction

MICROWAVE tomographic imaging has posed significant promise for medical imaging based on correlations between tissue electrical properties and clinically important pathologies. In general, tissue properties range from $\varepsilon_r \approx 5$ and $\sigma \approx 0.2$ S/m for fat and bone to $\varepsilon_r \approx 70$ and $\sigma \approx 2.5$ S/m for higher water-content tissue over the low microwave frequency range (300 to 3000 MHz) [1], [2]. Property variations have been noted for ischemic versus normal heart muscle [3], normal versus malignant breast tissue [4], [5], and normal bone versus leukemic marrow [6]. Additionally, the thermal dependence of tissue electrical conductivity is well known and may provide a means for noninvasively monitoring temperature during thermal therapies [1], [2], [7], [8]. However, efforts to exploit these microwave signatures have generally been disappointing due to limitations in data acquisition and lack of suitable imaging algorithms which can incorporate the high degree of three-dimensional (3-D) signal reflection and refraction associated with scattering from objects that are close in size to the wavelength of the interrogating wavefronts [9]–[12].

Due to the highly scattering nature of tissue, microwave radiation cannot be treated with straight-line propagation approximations as in X-ray computed tomography. In early two-dimensional (2-D) tomographic implementations, diffraction approaches were applied to linearize the reconstruction problem utilizing primarily Born and Rytov approximations [11], [13]. These were appealing at the time because images could be produced efficiently, given the limited computational power available. They were shown to be effective when the scattering objects were electrically small or when the contrast with the background was minimal [10], which is generally not the case for imaging of biological tissue.

Iterative approaches are well suited for nonlinear problems, but can be computationally expensive with respect to the multiplicity of field solutions that are required [14]. Numerous iterative methods have been successfully implemented in simulation, phantom, *ex vivo* and *in vivo* experiments to demonstrate the capabilities of microwave imaging. In simulation, 2-D imaging schemes have been reported by Joachimowicz *et al.* [14], Caorsi *et al.* [15], Semenov *et al.* [16] and Meaney *et al.* [17], among others. Phantom and *ex vivo* image reconstruction results have also been described by Semenov *et al.* [16], [18] and Meaney *et al.* [19], [20]. Preliminary *in vivo* experiments have been presented by Semenov *et al.* [21] for imaging the canine heart and by Meaney *et al.* for thermal imaging in the torso of small pigs [22] and in the human breast [23]. In general, these tomographic approaches have been found not to be restricted by wavelength criteria but rather by signal-to-noise limitations [24]. This is especially important in biomedical applications where the distance in tissue that a microwave signal can be transmitted is short and generally decreases as a function of frequency, imposing a premium on reducing the operating frequency while at the same time preserving imaging spatial resolution.

Alternatives to tomographic approaches include confocal imaging and passive radiometry. The former approach transmits a broadband pulse from a single antenna within an array and records the backscattered response [25], [26]. The signals are synthetically combined to focus sequentially at all points in the domain to produce a map of return-signal intensity. The

Manuscript received June 23, 2003; revised November 3, 2003. This work was supported in part by the National Institutes of Health (NIH) through the National Cancer Institute under Grant R01-CA55034. The Associate Editor responsible for coordinating the review of this paper and recommending its publication was R. Leahy. *Asterisk indicates corresponding author.*

*Q. Fang is with the Thayer School of Engineering, Dartmouth College, 8000 Cummings Hall, Hanover, NH 03755 USA (e-mail: qianqian.fang@dartmouth.edu).

P. M. Meaney, S. D. Geimer, A. V. Streltsov, and K. D. Paulsen are with the Thayer School of Engineering, Dartmouth College, Hanover, NH 03755 USA (e-mail: paul.m.meaney@dartmouth.edu; shireen.geimer@dartmouth.edu; anatoly.v.streltsov@dartmouth.edu; keith.d.paulsen@dartmouth.edu).

Digital Object Identifier 10.1109/TMI.2004.824152

spatial resolution is nominally related to the bandwidth of the applied signal pulse. This approach may prove useful in breast cancer detection where the electrical property contrast between normal background and malignant tissue is substantial [4], [5]. Passive radiometry has been applied to monitoring thermal profiles during hyperthermia treatment based on black body radiation detection [27] where depth resolution improvements can be achieved by using an increased number of operating frequencies. This approach is also utilized in breast cancer detection by sensing subtle temperature elevations related to the enhanced metabolic activity of tumor cells [28]. The system by Carr *et al.* has demonstrated an improved positive predictive value (the number of women with actual breast cancers with respect to the total number recommended for biopsy) of 41% in conjunction with standard mammographic screening versus 24% for mammography alone based on a recent study of 129 women.

While it is clear that electromagnetic field propagation is 3-D, most of the imaging and inverse scattering developments have been 2-D, largely because of the significant measurement and computational costs associated with 3-D imaging. Notwithstanding, it is important to study potential improvements that may be achieved by using algorithms which account for 3-D effects [29]. Several investigators have reported their early experience with 3-D algorithms [14], [21], [30]. While these efforts have broken important new ground in terms of introducing 3-D imaging concepts, there is a considerable amount of work that remains in order to establish 3-D microwave imaging as the current state-of-the-art. Further, 3-D investigations are needed to provide insight into the limitations of purely 2-D algorithms which have been more widely disseminated. The simulation studies reported in this paper represent an important step toward full 3-D image reconstruction while also providing a framework for exploring certain innovations that may lead to a viable near-real-time imaging approach in the future. Computational strategies employed here include: 1) a 3-D scalar model for the field propagation instead of full vector representation, 2) a block iterative matrix solver that efficiently computes the solution to multiple forward problems, simultaneously, 3) a 2-D parameter reconstruction approach incorporating the dual mesh scheme, and 4) an adjoint process to significantly reduce the computational costs of constructing the Jacobian matrix used to calculate the iterative image parameter updates. Utilizing a scalar field propagation model limits the forward electromagnetic field computational problem to a manageable size. The multiple right-hand side (RHS) iterative solver also significantly reduces computational costs along with the adjoint procedure which greatly decreases the effort at each iteration and the dual mesh scheme which substantially minimizes the amount of measured data required to achieve a successful inversion. To incorporate some of the important advances resulting from our 2-D studies, certain techniques such as the log-magnitude/phase minimization have also been implemented.

The remainder of the paper is organized into a theory and techniques section (Section II), which provides a summary of the underlying methodology. This is followed by the results (Section III), which report and analyze images recovered with the algorithm for various phantom experiments that are representative of cases previously studied with our 2-D algorithms. Metrics developed in the 2-D studies are applied to the output of these 3-D reconstructions to assess potential improvements. The results and innovations of the work are summarized in the concluding section of the paper (Section IV).

II. Theory and Techniques

The 3-D/2-D microwave imaging technique (3-D field solution driving 2-D property parameter estimation) is the solution approach to the inverse scattering problem described in this section. Here, the forward problem represents the calculation of the electric field for 1) the current estimate of the property distribution everywhere, including within the imaging zone, and 2) the known electromagnetic source configuration. Conversely, the inverse scattering problem generates the estimation of the property distribution in the imaging zone for a known 1) property distribution outside the imaging region, 2) electromagnetic source configuration and 3) measured electric field values at selected points. The Helmholtz problem is the governing equation for computing the interaction of electromagnetic fields with tissues and can be solved as a discrete set of linear algebraic equations. The inverse scattering problem is inherently nonlinear and best solved by iterative approaches. In this instance, we have applied a Gauss–Newton algorithm to reconstruct property estimates from synthetic measured data where computation of the forward electric field problem at each iteration is compared with the corresponding measured values to generate the property updates. In studying the 3-D imaging problem, algorithmic design choices for both the forward solution and property update procedure at each iteration are critical in developing a cost effective technique.

A. Forward Problem

Regardless of the approach chosen for computing the forward solution, the computational problem can grow quickly depending on the physical volume of the imaging domain and the spatial discretization of the numerical solution. We have chosen a scalar 3-D finite-element (FE) method as an approximation to the full vector field form developed by Paulsen *et al.* [31] which eliminates numerical parasites associated with 3-D vector FE approaches. The FE technique is appealing because the sparse nature of the associated matrix system significantly reduces the problem size both in terms of memory and CPU time requirements (assuming an efficient iterative solver is available). Utilizing the scalar version instead of its vector form also significantly reduces the problem size while potentially introducing only moderate errors when compared with the solution computed for all three components. This issue is briefly investigated by comparing scalar and vector field solutions in representative cases (See Section III-C). In the work described here, the cylindrical volume used to compute the forward solution extends radially beyond the circular array of driving antennas (oriented vertically) and several layers of FEs are used above and below the antenna cross-sectional plane to minimize interactions with finite boundaries resulting from mesh truncation (Fig. 1). Radiation boundary conditions

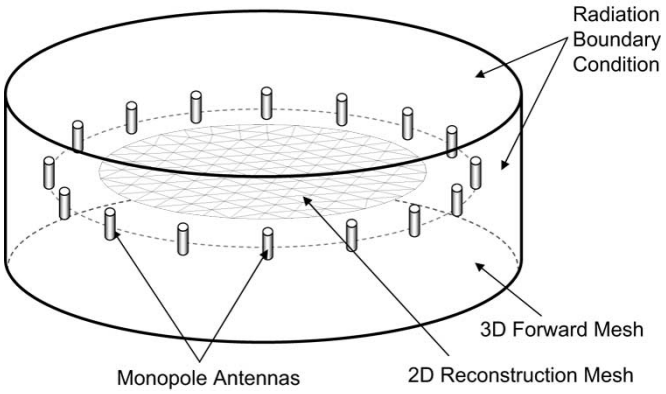

Fig. 1. Schematic of the 3-D/2-D imaging problem—the 2-D reconstruction area is centered within an array of 16 monopole antennas with the 3-D cylindrical volume extending radially beyond the antennas and a substantial distance above and below the 2-D imaging plane.

(RBCs) are applied to those surfaces to accurately represent unbounded field propagation while facilitating truncation of the problem to an acceptable size [32].

1) Three-Dimensional Scalar Model: To generate the scalar model of field propagation used in this paper, we start with the time-harmonic Maxwell's equations [assuming time dependence of $\exp(j\omega t)$]

$$\nabla \times \bar{H} = j\omega\varepsilon\bar{E} + \bar{J} \tag{1}$$

$$\nabla \times \bar{E} = -j\omega\mu\bar{H} \tag{2}$$

where $\bar{E}$ and $\bar{H}$ are the vector electric and magnetic fields generated by current density $\bar{J}$, respectively, ω is the radian frequency, ε is the electric permittivity, μ is the magnetic permeability and $j = \sqrt{-1}$. In the cases encountered here, ε is complex with $\varepsilon = \varepsilon_0(\varepsilon_r - j\varepsilon'')$ where ε_0 is the free space permittivity, ε_r is the relative permittivity, and ε'' is the relative imaginary component of the permittivity with $\varepsilon'' = (\sigma/\omega\varepsilon_o)$ where σ is the electrical conductivity. μ is equal to μ_0 (the free space permeability) since biological tissues are not magnetic. Combining (1) and (2) to eliminate $\bar{H}$ produces

$$\nabla \times (\nabla \times \bar{E}) - \omega^2\mu_0\varepsilon\bar{E} = -j\omega\mu_0\bar{J}. \tag{3}$$

The vector identity

$$\nabla \times \nabla \times \bar{U} = \nabla\nabla \cdot \bar{U} - \nabla^2\bar{U} \tag{4}$$

along with the relationship

$$\nabla \cdot \bar{D}(\bar{r}) = 0 \tag{5}$$

where $\bar{D}(\bar{r}) = \varepsilon(\bar{r})\bar{E}(\bar{r})$ is the electric flux density, which can be expanded to give

$$\nabla \cdot \bar{E}(\bar{r}) = -\frac{1}{\varepsilon(\bar{r})}\bar{E}(\bar{r}) \cdot \nabla\varepsilon(\bar{r}) \tag{6}$$

are used to produce

$$\nabla^2\bar{E}(\bar{r}) + k^2(\bar{r})\bar{E}(\bar{r}) + \nabla\left[\frac{\bar{E}(\bar{r}) \cdot \nabla k^2(\bar{r})}{k^2(\bar{r})}\right] = j\omega\mu_0\bar{J}(\bar{r}) \tag{7}$$

where $k^2(\bar{r}) = \omega^2\mu_0\varepsilon(\bar{r})$ is the complex wave number squared. Two assumptions are applied to simplify (7): 1) the electrical properties in the forward problem are invariant along the z-axis, i.e., $(\partial k^2(\bar{r}))/(\partial z) = 0$, (This assumption also occurs during 2-D reconstruction), and 2) the radiation field of the z-oriented dipole antennas comprising the imaging array can be reasonably approximated by TM polarization, i.e., $E_x = E_y = 0$ (although it is important to recognize that the presence of a geometrically complex object with z-axis electrical property variations will generated non zero transverse field components). The appropriateness of the latter approximation for the present situation is investigated in Section III. As a result, (7) becomes

$$\nabla^2 E_z(\bar{r}) + k^2(\bar{r})E_z(\bar{r}) = j\omega\mu_0 J_z(\bar{r}) \tag{8}$$

which is the final form of the field propagation model incorporated into the studies reported here.

The FE method is used to model the electric field distribution based on (8). Utilizing tetrahedral elements with linear basis functions, the weak form system of equations can be constructed by multiplying by a weighting function (Galerkin method), integrating the product over the entire domain and invoking the divergence theorem on the Laplacian term to produce

$$\langle \nabla E_z, \nabla\phi_\ell \rangle - \langle k^2 E_z, \phi_\ell \rangle - \oint_{\partial\Omega} \nabla E_z \cdot \hat{n}\phi_\ell \, ds = \langle -jw\mu_0 J_z, \phi_\ell \rangle \tag{9}$$

where $\langle , \rangle$ is the integration of the product of the two terms over the entire modeled volume, $\partial\Omega$ is the surface of that volume, ϕ_ℓ are the weighting functions, $\hat{n}$ is the unit normal vector to the volume surface. By satisfying (9) for the weighting functions associated with all nodes in the 3-D FE mesh, a system of N equations with N unknowns (the electric field values at all nodes) can be constructed and organized in matrix form

$$[A]\{E_z\} = \{b_z\} \tag{10}$$

where the coefficients of $[A]$ are comprised of

$$\langle \nabla\phi_i, \nabla\phi_\ell \rangle - \langle k^2\phi_i, \phi_\ell \rangle \tag{11}$$

and $\{b_z\}$ of

$$\langle -jw\mu_0 J_z(x,y)_i, \phi_\ell \rangle. \tag{12}$$

Note that the contribution from the surface integral in (9) is discussed in the following section. It is important also to note that $[A]$ contains all of the information pertaining to the electrical property distribution within the modeled zone while $\{b_z\}$ contains all of the source antenna data.

2) Radiation Boundary Conditions: The modeled region must be truncated at a finite distance to limit the problem size. However, it is essential that the imposition of boundary conditions (BCs) do not detract from the forward solution accuracy. Since the imaging experiments we perform are conducted in a tank filled with a lossy medium which minimizes the effects of signals reflecting off of the tank and liquid surfaces, RBCs

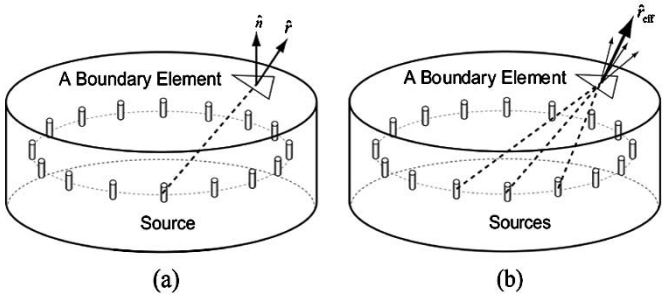

Fig. 2. Schematic of (a) the vector from a portion of a single line source to a boundary element on the cylindrical volume, and (b) the vectors from multiple antennas simultaneously projected to produce an effective $\hat{r}$ vector at the boundary element.

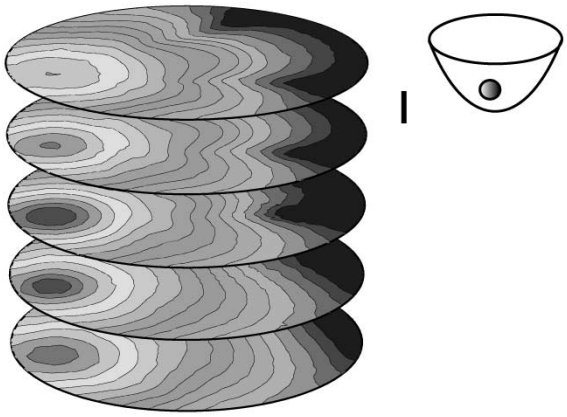

Fig. 3. Plots of the electric field magnitude at multiple planes due to a 900-MHz line source radiating into a saline medium with a breast-shaped object containing a tumor-like inclusion. Schematic of the antenna with respect to the breast are shown to the right.

were implemented to mimic the field radiation away from the imaging zone. The Sommerfeld radiation BC is described by

$$\lim_{r\to\infty} r\left(\frac{\partial E_z}{\partial r} - jkE_z\right) = 0 \tag{13}$$

on the surface of a 3-D sphere, S_r, with radius r where the sources and scatterers are assumed to be at the center of the sphere. We apply this to the cylindrical volume with radii computed from the antennas to the volume surface under the assumption that the substantial lossiness of the medium makes this approximation reasonable. From (13) we get

$$\nabla E_z|_{\partial\Omega} = jk\hat{r}E_z|_{\partial\Omega} \tag{14}$$

where $|_{\partial\Omega}$ denotes evaluation on the volume surface, $\partial\Omega$, and $\hat{r}$ is the unit vector in the direction emanating from a point on the antenna source to $\partial\Omega$ (Fig. 2). Equation (9) can then be re-written as

$$\langle \nabla E_z, \nabla\phi_\ell\rangle - \langle k^2 E_z, \phi_\ell\rangle - \oint_{\partial\Omega} jkE_z\hat{r}\cdot\hat{n}\phi_\ell\, ds = \langle -jw\mu_0 J_z, \phi_\ell\rangle. \tag{15}$$

Because the antennas are finite length, the direction of $\hat{r}$ at $\partial\Omega$ changes as a function of the section of the antenna that is referenced. To account for this nonlinear variation in the direction of $\hat{r}$, its direction is integrated along the antenna length to produce an effective $\hat{r}$, which is used in (15). Fig. 3 shows relative magnitude electric field contour plots for a single antenna radiating in a saline medium near a homogeneous breast-shaped object with a high contrast inclusion. For this heterogeneous region example, the scattering due to the breast object is appropriate but no distortions are discernible due to field interactions at the mesh truncation boundaries.

Several assumptions have been made in constructing (15) including the fact that 1) the imaging volume is a cylindrical instead of a spherical and 2) the sources are not at the geometric center of the volume. The second assumption has immediate impact on the surface integral term in (15). If $\hat{r}$ is taken as the unit vector from each individual source corresponding to J_z on the RHS of (15), matrix $[A]$ will vary for each transmitter. This has significant computational consequences since (10) must be solved independently for each source. However, an alternative approach is to construct the $\hat{r}\cdot\hat{n}$ product utilizing the weighted sum of $\hat{r}$'s from all source antennas in the array (even though only one is active at a time) [Fig. 2(b)]. In this way, the contribution from the surface integral in (15) becomes independent of the active antenna, making $[A]$ identical for all sources. Table I shows a summary of the computed forward electric field magnitude and phase differences at 500 and 900 MHz for a single transmitter averaged over the associated 15 receiver antennas. The top half of the table contains the differences in a homogeneous saline solution between the numerical case with $\hat{r}$ referenced just to the transmitter and the analytical solution while the row below lists the differences between the numerical model utilizing the BCs with $\hat{r}$ referenced just to the transmitter (ANT1) and to the average of the 16 antennas (ANT16), respectively. In general, the differences between the ANT1 and ANT16 cases were less than the differences between the ANT1 and the exact analytical solutions except for the phase at 500 MHz where, in fact, the ANT16 values were generally closer to the analytical solution than were the ANT1 results. It should be noted that the average phase difference for the 900-MHz ANT1 versus analytical solution is beginning to get relatively large suggesting that this computation is approaching the upper frequency limit where the discretization of this particular mesh is sufficient to generate accurate results. Essentially, this shows that any errors introduced by moving from the exact analytical solution to that of the ANT1 BC are more significant than that introduced by

TABLE I
AVERAGE 500- AND 900-MHz FORWARD SOLUTION MAGNITUDE (DECIBELS) AND PHASE (DEGREES) DIFFERENCES FOR SIGNALS COMPUTED AT THE 15 ASSOCIATED RECEIVERS FOR A SINGLE TRANSMITTER

A. ANT1-Analytical B. ANT1-ANT16 C. ANT1-ANT16		500M		900M	
		Mag (dB)	Phase (deg)	Mag (dB)	Phase (deg)
Homogeneous	A.	0.92	4.2	0.43	25.5
	B.	0.45	6.0	0.03	5.5
Breast-Like Target	C.	0.46	6.5	0.12	5.9

[1] Homogeneous saline solution:
(A.) 1 antenna BC's versus the analytical solution, and
(B.) 1 antenna BC's versus the averaged 16 antenna BC's;
[2] breast target in saline solution:
(C.) 1 antenna BC's versus the averaged 16 antenna BC's.

replacing the ANT1 BCs with the ANT16 BCs. To verify this in a more complicated situation, we computed the same ANT1 and ANT16 differences for the case where there was a high contrast, breast-like object with a tumor inclusion (for details, see Section III-B) suspended in the saline solution. In general, the differences were only slightly worse than those for the homogeneous case (in the magnitude at 900 MHz, the difference was actually larger but still much less than the difference for the homogeneous ANT1 case and exact analytical solution) as would be expected when computing the fields for a more complex object. Implementation of this concept of an effective $\hat{r} \cdot \hat{n}$ contribution is essential for facilitating the use of the multiple RHS implementation of the matrix system solver described in the next section.

3) Iterative Solver With Multiple Right Hand Sides: In general, the matrix $[A]$ in (10) is too large to compute by direct lower/upper triangular (LU) decomposition but is well suited to iterative solvers [33], of which the biconjugate gradient (BCG) and the quasiminimum residual (QMR) methods are two of the most common. We have focused on the QMR method in this paper because it has been demonstrated to be superior to the BCG approach for applications involving large sparse matrices [34]. A number of strategies can be applied to precondition $[A]$ in order to cluster its eigenvalues which has the intended consequence of accelerating solution convergence [35]. Possible options include the incomplete Cholesky and the incomplete LU (ILU) preconditioners of which the latter was chosen because of its superior performance [33]. The QMR routine can be implemented in block form utilizing the block Lanczos algorithm to process multiple RHS vectors of (10), simultaneously. We performed several studies to determine whether the grouping of specific RHS vectors along with the block size had any effect on the solution convergence rate. In general, grouping RHS vectors corresponding to adjacent antennas provided faster convergence than when antenna vectors were arranged in random order. In addition, the size of the block had a significant impact on the convergence rate. Fig. 4 shows a plot of solution time per RHS vector versus block size for the configuration in Fig. 2(b) with 10 571 nodes and 54 720 tetrahedral elements. In this case, 16 antennas on a 15-cm-diameter circle in a single plane were used to generate the source fields. The convergence time per RHS is minimum at the block size of seven. We generally used a size of eight as a convenient denominator for organizing the complete set of antennas with only nominal degradation in solution time.

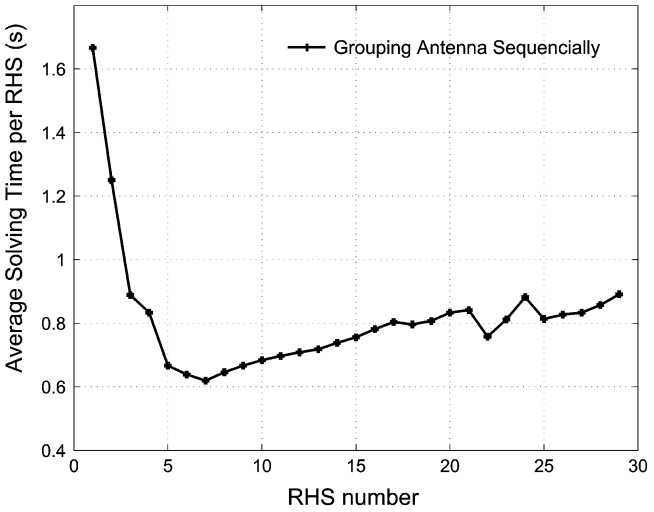

Fig. 4. Plot of the forward problem computation time per source antenna as a function of block size (number of right hand sides computed simultaneously) when the block QMR solver is used.

B. Image Reconstruction

Inversion utilizes a Gauss–Newton iterative approach for reconstructing permittivity and conductivity maps of a desired imaging zone. In general, the number of parameters that can be reconstructed is proportional to the amount of measurement data—in this case the number of transmit antennas multiplied by the number of receive antennas associated with each transmitter. For practical data acquisition systems, this imposes a significant constraint on the number of reconstruction parameters. We studied a problem where the property distribution was 2-D, i.e., the imaging targets were essentially cylinders with uniform properties in the axial direction (of the modeled volume). We applied the dual mesh scheme such that the spatial discretization of the parameter (coarse) mesh was considerably less refined than that of the 3-D field (fine) mesh. While the fine mesh is largely defined by the sampling requirements necessary to maintain accurate field computation, the property variation within the target can be quite different. This approach is generalizable to a full 3-D parameter reconstruction to be developed and evaluated at a later date which will be based on a 3-D forward/3-D reconstruction mesh pair and demand more measurement data compatible with an increasing number of parameters to be estimated. The 2-D reconstruction also limits problem size and significantly reduces computation time.

Our previous 2-D approach utilized direct differentiation of the governing field equation for constructing the Jacobian matrix required in the process of updating the property distribution at each iteration [17], [36]. The approach generates matrix back-substitutions of (10) for RHSs associated with every reconstruction parameter node for each transmitter, respectively. However, the principle of reciprocity (electric field value transmitted from antenna A and received at antenna B equals the value transmitted from B and received at A) can be exploited to compute each element of the Jacobian matrix through an inner product of the field distributions due to two antennas (already calculated as part of the forward solution) with a fixed weighting vector (the adjoint method [37]) that can be efficiently precomputed. This inner product calculation is an $\vartheta(N)$ operation while the back-substitutions are $\vartheta(N^2)$, providing a substantial time savings.

1) Dual Mesh Scheme: In the Gauss–Newton iterative approach utilized in the 3-D/2-D algorithm, the electrical properties, k^2 (whose distribution is represented over the 2-D parameter mesh), are updated at each iteration, γ, by the relationship

$$\left\{k^2_{\gamma+1}\right\} = \left\{k^2_{\gamma}\right\} + \left\{\Delta k^2\right\} \tag{16}$$

where $\{\Delta k^2\}$ is the property update and

$$k^2(x,y) = \sum_{\tau=1}^{M} k^2_{\tau}\varphi_{\tau}(x,y) \tag{17}$$

with k_τ^2 being the values of k^2 at the parameter nodes and φ_τ being the set of linear basis functions for the parameter mesh. Utilizing a truncated Taylor series representation, the electric field distribution can be expressed as

$$\{E^{\text{exact}}\} = \{E^{\text{approx}}\} + \left[\frac{\partial E^{\text{approx}}}{\partial k^2}\right]\{\Delta k^2\} \tag{18}$$

where $\{E^{\text{exact}}\}$ and $\{E^{\text{approx}}\}$ are the exact and approximated electric field distributions and $[(\partial E)/(\partial k^2)]$ is the derivative of the electric field with respect to the property values. Replacing the exact term with the measured field quantity, and the approximated value with the computed solution and rearranging yields

$$\left[\frac{\partial E}{\partial k^2}\right]\{\Delta k^2\} = \{E^{\text{meas}} - E^{\text{comp}}\} \tag{19}$$

where $[(\partial E/\partial k^2)]$ is the Jacobian matrix. Differentiating (10) with respect to k_τ^2 (value at parameter mesh node τ) produces

$$[A]\left\{\frac{\partial E}{\partial k_\tau^2}\right\} = -\left[\frac{\partial A}{\partial k_\tau^2}\right]\{E\} \tag{20}$$

which is solved for each parameter node for every antenna source. $[A]$ and $\{E\}$ are already determined at each iteration as part of the field solution for the current property estimate.

The matrix $[(\partial A)/(\partial k_\tau^2)]$ is sparse with terms defined by

$$\frac{\partial \alpha_{i,\ell}}{\partial k_\tau^2} = -\langle \phi_i \phi_\ell \varphi_\tau \rangle \tag{21}$$

where ϕ_i and ϕ_ℓ are the basis functions on the fine 3-D field mesh while φ_τ is the basis function for the coarse 2-D parameter mesh. The integrations are performed over the portion of the 3-D fine mesh where basis function φ_τ is nonzero (accomplished by projecting the 3-D coordinates of ϕ_i and ϕ_ℓ onto the 2-D parameter mesh). For the nonzero contributions in (21), the efficiency of their calculation is expedited by generating mapping relationships between the coordinates and basis functions of both meshes in a manner similar to that previously reported [36].

2) Adjoint Method: The expression for the Jacobian matrix elements can also be written as

$$\mathbf{J}(s,r,\tau) = \left\langle \frac{\partial E_s}{\partial k_\tau^2}, \delta(x_r, y_r) \right\rangle \tag{22}$$

which is the derivative of the electric field with respect to the electrical properties at node τ at measurement site, r, for radiation source at s, where δ is the Dirac delta function. If the RHS of (20) is considered to be an effective source, $\{b_{\text{eff}}\}$, where

$$[A]\left\{\frac{\partial E_s}{\partial k_\tau^2}\right\} = -\left[\frac{\partial A}{\partial k_\tau^2}\right]\{E_s\} = \{b_{\text{eff}}\} \tag{23}$$

$\{(\partial E_s)/(\partial k_\tau^2)\}$ can be interpreted as the "field distribution" due to source $\{b_{\text{eff}}\}$. If an auxiliary source, $\{b_r\}$, is applied at the receiver location, the resultant field distribution $\{E_r\}$ can be computed by

$$[A]\{E_r\} = \{b_r\} = \langle -j\omega\mu_0 J_r, \phi_\ell \rangle \tag{24}$$

where $\{J_r\}$ is the source current at this antenna which can be rewritten more specifically as

$$J_r = |J_r| \cdot \delta(x_r, y_r) \tag{25}$$

to emphasize its local support. Reciprocity ensures that

$$\langle b_r, E_s \rangle = \langle b_s, E_r \rangle \tag{26}$$

which in terms of the effective and auxiliary sources and fields requires that

$$\left\langle b_r, \frac{\partial E_s}{\partial k_\tau^2} \right\rangle = \langle b_{\text{eff}}, E_r \rangle \tag{27}$$

or equivalently from (21) and (23), that

$$\left\langle \frac{\partial E_s}{\partial k_\tau^2}, -j\omega\mu_0 |J_r| \delta(x_r, y_r) \right\rangle = \langle \langle \phi_i \phi_\ell \varphi_\tau \rangle E_s, E_r \rangle \tag{28}$$

which simplifies to

$$\left\langle \frac{\partial E_s}{\partial k_\tau^2}, \delta(x_r, y_r) \right\rangle = -\left\langle \frac{\langle \phi_i \phi_\ell \varphi_\tau \rangle}{j\omega\mu_0 |J_r|} E_s, E_r \right\rangle. \tag{29}$$

The left-hand side of (29) is precisely the term-by-term definition of the Jacobian matrix given in (22). Note that the inner product, or weight, $\langle \phi_i \phi_\ell \varphi_\tau \rangle$ is only a function of the fine and coarse mesh pair and can be precomputed and stored for later use. Therefore, evaluating the coefficients of the Jacobian, $\mathbf{J}$, involves only an inner product of field distributions (which are already computed at each iteration) multiplied by the weight which is an $\vartheta(N)$ operation compared with the $\vartheta(N^2)$ operation involved with solving for all permutations of sources, s, and reconstruction parameters, τ. As N increases, computational savings become considerable. Note that (29) is general and applicable to both 2-D and 3-D reconstruction problems.

III. Results

We have organized several experiments utilizing simulated measurement data to demonstrate the viability of the 3-D/2-D algorithm. While previous implementations of our 2-D scheme (2-D/2-D) have utilized innovations such as nonactive antenna compensation [23], [38] and conformal meshing [39], the scope of the investigations reported here center on computational efficiency, suitability of convergence behavior and whether there are improvements over the 2-D/2-D approach with respect to metrics devised to quantify 3-D wave propagation effects. Specifically, in Sections III-A and III-B, we have purposely eliminated the issue of data-model mismatch caused by using the scalar field approximation through the incorporation of simulated measurements which were generated by the scalar model. This synthetic data set also assumed no measurement noise. The intent of these studies is to highlight the ideal performance of the inversion algorithm prior to provoking any image quality degradations resulting from modeling error. In the spirit of establishing the ideal performance, we computed the measurement data on the same mesh employed for image recovery in these simulations. In Section III-C, on the other

hand, full vector field solutions were produced on a different high resolution mesh in order to construct the synthetic measurement data for image reconstruction which includes the effects of scalar model approximation. We also quantify the differences that can be expected between the 3-D vector and scalar models under representative conditions at the start of this section.

For all of the imaging experiments described, the 3-D FE region is an 18-cm-diameter cylinder with a height of 5 cm comprised of 11 uniform layers with a total of 10 571 nodes and 54 720 tetrahedral elements. The circular array (7.1-cm radius) of 16 antennas (1-cm length) is concentric within the vertical axis of the cylindrical FE mesh. In each imaging experiment, 16 transmitters were used while signals were received at nine opposing antennas for a total of 144 measurements. The 2-D image reconstruction mesh was a 12-cm-diameter circle concentric with the cylindrical volume comprised of 126 nodes and 214 triangular elements. For the reconstruction process, a hybrid regularization procedure combining Tikhonov $(\alpha = 0.5)$ and Marquardt (λ fixed at 0.1) schemes [40] was used in conjunction with a spatial filter applied at each iteration to remove high frequency variations through an averaging factor of 0.1 [40]. In all cases, the images converged to a stable solution within about six iterations which required approximately 1 min to execute on a Compaq Alpha 833-MHz ES40 workstation. By comparison, the 2-D/2-D algorithm processed a similar image reconstruction in 30 s for six iterations on the same machine. For the images presented in Sections III-A and III-B, the background medium was 0.9% saline ($\varepsilon_r = 77$ and $\sigma = 1.7$ S/m) with an operating frequency of 900 MHz. The experiments in Section III-C utilized a range of backgrounds to illustrate the influence of contrast on 3-D effects. All of these reconstructions started from an initial estimate consisting of the values for the homogeneous background.

A. Simple Cylindrical Phantom

Fig. 5(a) shows the 900-MHz reconstructed images of a 2.9-cm-diameter cylinder (approximated as a hexagonal shape best fit to the reconstruction parameter mesh) with $\varepsilon_r = 38.5$ and $\sigma = 0.85$ S/m for a contrast of 1:2 with the background properties. Both the permittivity and conductivity distributions are recovered quite well with only minor artifacts appearing in the conductivity image background. Transects through both images plotted in Fig. 5(b) illustrate the uniformity of the background recovery along with the position and size of the inclusion with respect to the exact distribution (also shown). It is interesting to note that the recovered properties underestimate those of the actual object in the center. This may be a consequence of the spatial filtering which restrains the algorithm from exactly recovering a property step-distribution at the object background interface, forcing the algorithm to compensate for this limitation by exaggerating the properties in the center of the object.

B. Breast-Like Cylindrical Phantom

Fig. 6(a) shows the 900-MHz permittivity and conductivity images recovered for a centered breast-like region with an inclusion. The large 8-cm-diameter cylinder (which is about

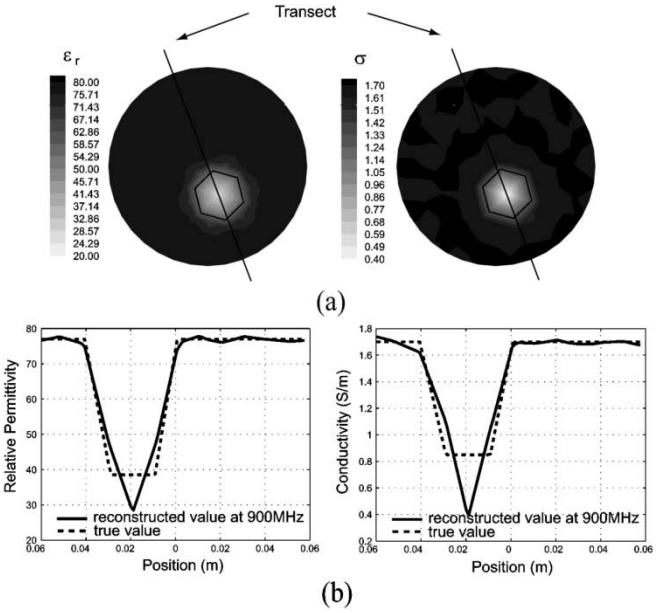

Fig. 5. (a) The 900-MHz reconstructed permittivity and conductivity images for a 2.9-cm-diameter cylinder within a homogeneous saline background, and (b) the associated property transects through the imaging domain including the recovered object compared with the actual distributions.

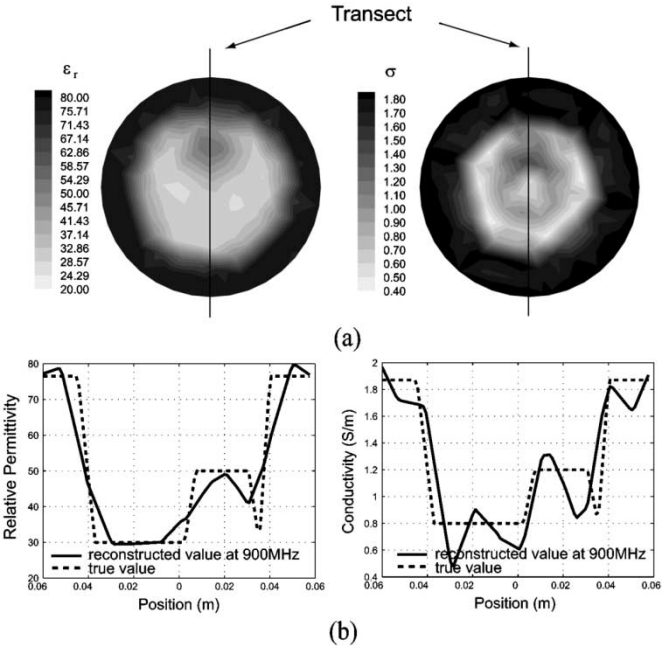

Fig. 6. (a) The 900-MHz reconstructed permittivity and conductivity images for an 8-cm-diameter breast-like phantom with a 3-cm-diameter inclusion within a homogeneous saline background, and (b) the associated property transects through the imaging domain including the recovered breast and inclusion compared with the actual distributions.

2.2λ) properties were $\varepsilon_r = 30.0$ and $\sigma = 0.8$ S/m while those for the offset, 3-cm-diameter inclusion were $\varepsilon_r = 50.0$ and $\sigma = 1.2$ S/m. In contrast to the previous example, our log-magnitude/unwrapped phase minimization was used for this case because the standard complex form diverged as a result of the high proportion of measured phase wrapping [41]. The excessive phase wrapping of the scattered fields is directly related to the target size, contrast and operating frequency.

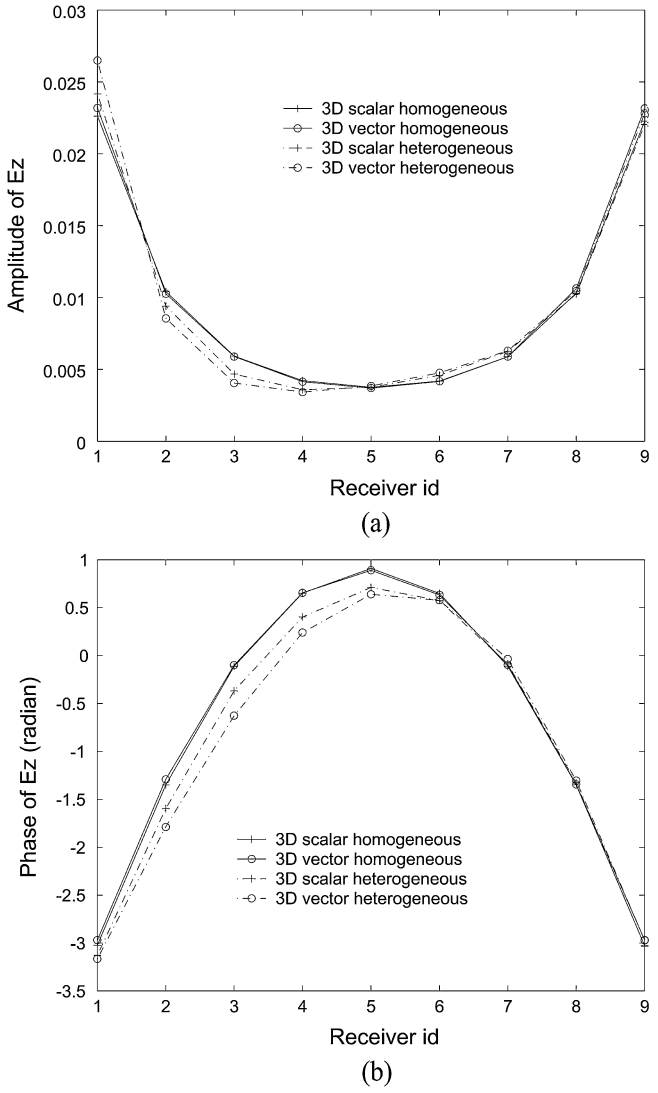

Fig. 7. Comparison of the (a) magnitude and (b) phase of the fields at antenna array measurement sites for the 3-D scalar and vector propagation models in a homogeneous background and a background containing a spherical object within the array.

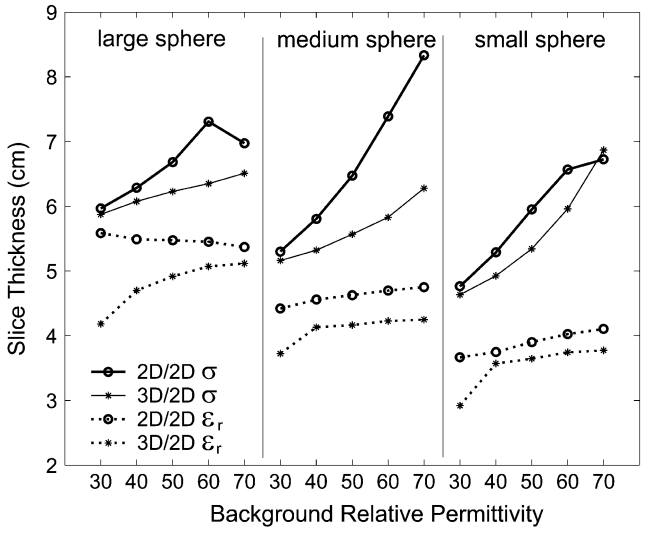

Fig. 8. Plots of the slice thickness computed at 900 MHz for the recovered permittivity and conductivity images using 4.6, 3.6, and 2.5-cm-diameter spheres ($\varepsilon_r = 20.0$, and $\sigma = 0.18$ S/m) as a function of background permittivity ($\sigma = 1.78$ S/m). Plots are compared with corresponding results using the 2-D/2-D algorithm.

It is important that concepts successfully developed in the 2-D/2-D approach extend to the 3-D/2-D implementation.

From the image pair in Fig. 6, it is clear that the permittivity component is recovered more accurately than its conductivity counterpart. For instance, there is a considerably higher level of artifacts in both the background properties and internal breast composition for the conductivity image and the reconstructed breast geometry appears smaller for the conductivity relative to the permittivity map. These observations are generally consistent with previously reported findings [19]. For the plots of the recovered properties along the vertical transects through the phantom [Fig. 6(b)], previous observations are also confirmed in that both images recover accurate property profiles, although the permittivity component generally has fewer artifacts. Additionally, it also appears that the location of the recovered inclusion is correct for the permittivity image while it is noticeably skewed to one side in the conductivity case. This is again consistent with previously reported images obtained from the 2-D/2-D configuration [39], and is clearly exacerbated by the high contrast background.

C. Reduction in 3-D Propagation Effects

Prior to investigating image reconstruction differences in a 3-D problem between our existing 2-D/2-D algorithm and the 3-D/2-D approach developed here, we begin this section by quantifying the differences in the underlying 3-D scalar model of field propagation with its more appropriate 3-D vector version under two representative conditions—a homogeneous imaging volume and an heterogeneous volume. Fig. 7 shows field values computed for the 3-D scalar and full vector models at the imaging array antenna sites under 500-MHz illumination of a homogenous and heterogeneous volume. In the homogeneous case, a background medium with $\varepsilon_r = 70$ and $\sigma = 1.7$ S/m was used while in the heterogeneous problem this same background included an off-centered sphere ($r = 1.78$ cm, 2.54 cm offset from the center of the antenna array) with $\varepsilon_r = 20$ and $\sigma = 0.18$ S/m. The solutions illustrated in Fig. 9 result in mean amplitude differences of about 0.4% and 1.2% in the homogeneous and heterogeneous problems respectively and a mean difference of 1.5° and 5.4° in phase in the two cases.

A previous study based on the 2-D/2-D algorithm presented results utilizing a metric to estimate the imaging slice thickness [29] in order to quantify imaging artifacts due to 3-D field propagation effects. We present data here which directly compares the 3-D/2-D and 2-D/2-D algorithms in terms of this measure. The simulated scattered data was computed using a full FE 3-D vector formulation [31], [42] at 900 MHz. The study involved raising low permittivity spheres of different diameters through the imaging plane defined by the array of monopole antennas. Permittivity and conductivity images were recovered for each sphere (large: 4.6-cm diameter, about 1.3λ; medium: 3.6-cm diameter about 1λ; small: 2.5-cm diameter,

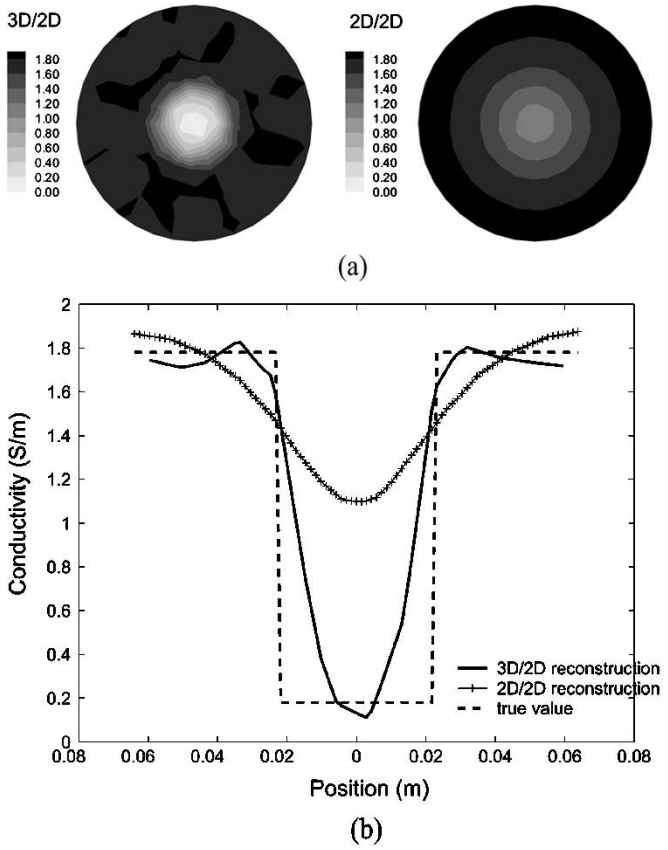

Fig. 9. (a) Plots of the reconstructed conductivity for the large sphere (4.6-cm diameter) in background $\varepsilon_r = 60$ at 900 MHz by 3-D/2-D and 2-D/2-D methods, (b) transects of the reconstructed conductivity profiles together with the true value of the distribution.

about 0.7λ) at each vertical position separated in 1.27-cm-increments. The electrical properties of the spheres were $\varepsilon_r = 20.0$ and $\sigma = 0.18$ S/m while the relative permittivity of the background varied from 30 to 70 with the conductivity fixed at 1.78 S/m. As an indication of averaging effect along the z-axis due to 3-D microwave propagation, imaging slice thicknesses derived from the recovered sphere half width and peak values of its estimated properties (see Meaney *et al.* [29] for a complete definition) were computed for both the permittivity and conductivity, for all three spheres and over the complete range of background permittivities, respectively. Fig. 8 compares plots of the imaging slice thickness as a function of background permittivity for both the 2-D/2-D and 3-D/2-D algorithms. For almost all cases, the slice thickness for the 3-D/2-D algorithm is smaller. In general, the slice thickness is greater for larger sized spheres and the permittivity slice thickness is smaller than in the corresponding conductivity images. The conductivity thickness decreases consistently for both algorithms and appears to converge to similar values for the lowest background permittivity. The permittivity thicknesses for the 2-D/2-D algorithm are relatively flat as a function of background permittivity—decreasing slightly for the large sphere and increasing slightly for the two smaller spheres. In contrast, the permittivity thicknesses for the 3-D/2-D cases consistently decrease with respect to a lower background permittivity. In general, both algorithms demonstrate improvement in reducing the imaging slice thicknesses with reduced background contrast, where the 3-D/2-D algorithm produces consistently smaller values and is generally better at handling larger targets. As a visual example of the 3-D/2-D algorithm enhancement in a representative case, Fig. 9 shows a pair of conductivity images obtained from the reconstructions of the large sphere with the antenna array positioned in the azimuthal plane by the two methods. The improvement is evident in terms of the sharper and more accurate contrast with the background that is achieved with the 3-D/2-D method.

IV. Conclusion

We have implemented a 3-D scalar field solution/2-D Gauss–Newton iterative parameter inversion algorithm (3-D/2-D) for microwave imaging. Various strategies including exploitation of a 3-D scalar formulation and a truncated mesh with RBCs were deployed to limit the computational overhead of the problem. Additionally, as an important initial step, we developed a 2-D reconstruction procedure that is integrated with the 3-D field solution. This is significant in a practical sense because measurement data is a precious commodity and the number of parameters that can be independently estimated is proportional to the amount of measurement data which is available. Restricting the parameter reconstruction to 2-D allows this new algorithm to be applied to the limited microwave signal channels now in place [23]. However, it is also important because the 2-D inversion portion of the algorithm has been developed to readily generalize to a full 3-D reconstruction when the requisite amount of measurement data can be acquired. Implementation of the adjoint method to dramatically accelerate computation of the Jacobian matrix has made 3-D approaches much more attainable.

The range of results presented here demonstrate the capabilities of the 3-D/2-D algorithm in a variety of settings—specifically in a simple 2-D cylinder and a more complex, large, breast-like cylindrical geometry. In addition, a full set of experiments were performed to illustrate that the 3-D/2-D algorithm is an overall improvement over the 2-D/2-D algorithm in terms of reducing previously observed 3-D artifacts. In general, these results are encouraging and set the stage for development of more advanced 3-D/3-D methods to be used in conjunction with more sophisticated data acquisition systems.

References

[1] C. Gabriel, S. Gabriel, R. W. Lau, and E. Corthout, "The dielectric properties of biological tissues: Parts I, II, and III," *Phys. Med. Biol.*, vol. 41, pp. 2231–2249, 1996.

[2] F. A. Duck, *Physical Properties of Tissues: A Comprehensive Reference Book*, London, U.K.: Academic, 1990.

[3] S. Y. Semenov, R. H. Svenson, and G. P. Tatsis, "Microwave spectroscopy of myocardial ischemia and infarction: 1. Experimental study," *Ann. Biomed. Eng.*, vol. 28, pp. 48–54, 2000.

[4] S. S. Chaudhary, R. K. Mishra, A. Swarup, and J. M. Thomas, "Dielectric properties of normal and malignant human breast tissues at radiowave and microwave frequencies," *Ind. J. Biochem. Biophys.*, vol. 21, pp. 76–79, 1984.

[5] W. T. Joines, Y. Zhang, C. Li, and R. L. Jirtle, "The measured electrical properties of normal and malignant human tissues from 50 to 900 MHz," *Med. Phys.*, vol. 21, pp. 547–50, 1994.

[6] D. Colton and P. Monk, "The detection and monitoring of leukemia using electromagnetic waves: Numerical analysis," *Inverse Prob.*, vol. 11, pp. 329–342, 1995.

[7] R. Pethig, "Dielectric properties of biological materials: Biophysical and medical applications," *IEEE Trans. Elect. Insulation*, vol. EI-19, pp. 453–474, 1984.

[8] E. C. Burdette, F. L. Cain, and J. Seals, "In-situ tissue permittivity at microwave frequencies: Perspective, techniques, results," *Medical Applications of Microwave Imaging*, 1986.

[9] J. C. Bolomey, J. Izadnegahdar, L. Jofre, C. H. Pichot, G. Peronnet, and M. Solaimani, "Microwave diffraction tomography for biomedical applications," *IEEE Trans. Microwave Theory Tech.*, vol. MTT-30, pp. 1990–2000, 1982.

[10] M. Slaney, A. C. Kak, and L. E. Larsen, "Limitations of imaging with first-order diffraction tomography," *IEEE Trans. Microwave Theory Tech.*, vol. MTT-32, pp. 860–874, 1984.

[11] L. Jofre, M. S. Hawley, A. Broquetas, E. de los Reyes, M. Ferrando, and A. R. Elias-Fuste, "Medical imaging with a microwave tomographic scanner," *IEEE Trans. Biomed. Eng.*, vol. 37, pp. 303–312, Mar. 1990.

[12] R. Maini, M. F. Iskander, and C. H. Durney, "On electromagnetic imaging using linear reconstruction techniques," *Proc. IEEE*, vol. 68, pp. 1550–1552, 1980.

[13] A. Broquetas, J. Romeu, J. M. Rius, A. R. Elias-Fuste, A. Cardama, and L. Jofre, "Cylindrical geometry: A further step in active microwave tomography," *IEEE Trans. Microwave Theory Tech.*, vol. 39, pp. 836–844, May 1991.

[14] N. Joachimowicz, C. Pichot, and R. Hugonin, "Inverse scattering: An iterative numerical method for electromagnetic imaging," *IEEE Trans. Antennas Propagat.*, vol. 39, pp. 1742–1752, Dec. 1991.

[15] S. Caorsi, G. L. Gragnani, and M. Pastorino, "A multi-view microwave imaging system for two dimensional penetrable objects," *IEEE Trans. Microwave Theory Tech.*, vol. 39, pp. 845–851, May 1991.

[16] S. Y. Semenov, R. H. Svenson, A. E. Boulyshev, A. E. Souvorov, V. Y. Borisov, Y. Sizov, A. N. Starostin, K. R. Dezern, G. P. Tatsis, and V. Y. Baranov, "Microwave tomography: Two-dimensional system for biological imaging," *IEEE Trans. Biomed. Eng.*, vol. 43, pp. 869–877, Sept. 1996.

[17] P. M. Meaney, K. D. Paulsen, and T. P. Ryan, "Two-dimensional hybrid element image reconstruction for TM illumination," *IEEE Trans. Antennas Propagat.*, vol. 43, pp. 239–247, Mar. 1995.

[18] S. Y. Semenov, R. H. Svenson, A. E. Bulyshev, A. E. Souvorov, A. G. Nazarov, Y. E. Sizov, A. V. Pavlovsky, V. Y. Borisov, B. A. Voinov, G. I. Simonova, A. N. Starostin, V. G. Posukh, G. P. Tatsis, and V. Y. Baranov, "Three-dimensional microwave tomography: Experimental prototype of the system and vector born reconstruction method," *IEEE Trans. Biomed. Eng.*, vol. 46, pp. 937–946, Aug. 1999.

[19] P. M. Meaney, K. D. Paulsen, and J. T. Chang, "Near-field microwave imaging of biologically based materials using a monopole transceiver system," *IEEE Trans. Microwave Theory Tech.*, vol. 46, pp. 31–45, Jan. 1998.

[20] P. M. Meaney, K. D. Paulsen, J. T. Chang, and M. Fanning, "Compensation for nonactive array element effects in a microwave imaging system: Part II—Imaging results," *IEEE Trans. Med. Imag.*, vol. 18, pp. 508–518, June 1999.

[21] S. Y. Semenov, R. H. Svenson, A. E. Bulyshev, A. E. Souvorov, A. G. Nazarov, Y. E. Sizov, V. G. Posukh, A. Pavlovsky, P. N. Repin, A. N. Starostin, B. A. Voinov, M. Taran, G. P. Tatsis, and V. Y. Baranov, "Three-dimensional microwave tomography: Initial experimental imaging of animals," *IEEE Trans. Biomed. Eng.*, vol. 49, pp. 55–63, Jan. 2002.

[22] P. M. Meaney, M. W. Fanning, K. D. Paulsen, D. Li, S. A. Pendergrass, Q. Fang, and K. L. Moodie, "Microwave thermal imaging: Initial *in vivo* experience with a single heating zone," *Int. J. Hypertherm.*, vol. 19, pp. 617–641, 2003.

[23] P. M. Meaney, M. W. Fanning, D. Li, S. P. Poplack, and K. D. Paulsen, "A clinical prototype for active microwave imaging of the breast," *IEEE Trans. Microwave Theory Tech.*, vol. 48, pp. 1841–1853, Nov. 2000.

[24] J. C. Bolomey, C. Pichot, and G. Gaboriaud, "Planar microwave imaging camera for biomedical applications: Critical and prospective analysis of reconstruction algorithms," *Radio Sci.*, vol. 26, pp. 541–550, 1991.

[25] S. C. Hagness, A. Taflove, and J. E. Bridges, "Two-dimensional FDTD analysis of a pulsed microwave confocal system for breast cancer detection: Fixed-focus and antenna-array sensors," *IEEE Trans. Biomed. Eng.*, vol. 45, pp. 1470–1479, Dec. 1998.

[26] E. C. Fear, X. Li, S. C. Hagness, and M. A. Stuchly, "Confocal microwave imaging for breast cancer detection: Localization of tumors in three dimensions," *IEEE Trans. Biomed. Eng.*, vol. 49, pp. 812–822, Aug. 2002.

[27] S. Jacobsen and P. R. Stauffer, "Nonparametric 1-D temperature restoration in lossy media using Tikhonov regularization on sparse radiometry data," *IEEE Trans. Biomed. Eng.*, vol. 50, pp. 178–188, Feb. 2003.

[28] K. L. Carr, P. Cevasco, P. Dunlea, and J. Shaeffer, "Radiometric sensing: An adjuvant to mammography to determine breast biopsy," in *Proc.IEEE MTT Symp.*, Boston, MA, 2000, pp. 929–932.

[29] P. M. Meaney, K. D. Paulsen, S. Geimer, S. Haider, and M. W. Fanning, "Quantification of 3-D field effects during 2-D microwave imaging," *IEEE Trans. Biomed. Eng.*, vol. 49, pp. 708–720, July 2002.

[30] S. Caorsi, A. Massa, and M. Pastorino, "A numerical solution to full-vector electromagnetic scattering by three-dimensional nonlinear bounded dielectrics," *IEEE Trans. Microwave Theory Tech.*, vol. 43, pp. 428–436, Feb. 1995.

[31] K. D. Paulsen, X. Jia, and J. M. Sullivan Jr., "Finite element computations of specific absorption rates in anatomically conforming full-body models for hyperthermia treatment analysis," *IEEE Trans. Biomed. Eng.*, vol. 40, pp. 933–945, Sept. 1993.

[32] T. B. A. Senior and J. L. Volakis, *Approximate Boundary Conditions in Electromagnetics*, London, U.K.: Inst. Elect. Eng., 1995.

[33] W. E. Boyse and A. A. Seidl, "A block QMRmethod for computing multiple simultaneous solutions to complex symmetric systems," *SIAM J. Sci. Comput.*, vol. 17, pp. 263–274, 1996.

[34] R. W. Freund, "Conjugate gradient type methods for linear systems with complex symmetric coefficient matrices," *SIAM J. Sci. Statist. Comput.*, vol. 13, pp. 425–448, 1992.

[35] G. H. Golub and C. F. van Loan, *Matrix Computations*. Baltimore, MD: The Johns Hopkins Univ. Press, 1989.

[36] K. D. Paulsen, P. M. Meaney, A. Hartov, and R. K. Crane, "An active microwave imaging system for reconstruction of 2-D electrical property," *IEEE Trans. Biomed. Eng.*, vol. 42, pp. 1017–1026, Oct. 1995.

[37] C.-T. Liauh, R. G. Hills, and R. B. Roemer, "Comparison of the adjoint and influence coefficient methods for solving the inverse hyoperthermia problem," *J. Biomech. Eng.*, vol. 115, pp. 63–71, 1993.

[38] K. D. Paulsen and P. M. Meaney, "Nonactive antenna compensation for fixed-array microwave imaging. I. Model development," *IEEE Trans. Biomed. Eng.*, vol. 18, pp. 496–507, June 1999.

[39] D. Li, P. M. Meaney, and K. D. Paulsen, "Conformal microwave imaging for breast cancer detection," *IEEE Trans. Microwave Theory Tech.*, vol. 51, pp. 1179–1186, Apr. 2003.

[40] P. M. Meaney, E. Demidenko, N. K. Yagnamurthy, D. Li, M. W. Fanning, and K. D. Paulsen, "A two-stage microwave image reconstruction procedure for improved internal feature extraction," *Med. Phys.*, vol. 28, pp. 2358–2369, 2001.

[41] P. M. Meaney, K. D. Paulsen, B. W. Pogue, and M. I. Miga, "Microwave image reconstruction utilizing log-magnitude and unwrapped phase to improve high-contrast object recovery," *IEEE Trans. Med. Imag.*, vol. 20, pp. 104–116, Feb. 2001.

[42] K. D. Paulsen, S. Geimer, J. Tang, and W. E. Boyse, "Optimization of pelvic heating rate distributions with electromagnetic phased arrays," *Int. J. Hypertherm.*, vol. 15, pp. 157–166, 1999.